The Astrophysical Journal, 927:146 (10pp), 2022 March 10 https://doi.org/10.3847/1538-4357/ac4601

The Importance of Horizontal Poynting Flux in the Solar Photosphere

Suzana S. A. Silva[1,2], Mariarita Murabito[3], Shahin Jafarzadeh[4,5], Marco Stangliani[6], Gary Verth[7], Istvan Ballai[7], and Viktor Fedun[1]

[1] Plasma Dynamics Group, Department of Automatic Control and Systems Engineering, University of Sheffield, Sheffield, UK; suzana.silva@sheffield.ac.uk
[2] Department of Physics, Aeronautics Institute of Technology, São José dos Campos, Brazil
[3] INAF—Osservatorio Astronomico di Roma, Via Frascati, 33 Monte Porzio Catone, RM, I-00078, Italy
[4] Max Planck Institute for Solar System Research, Justus-von-Liebig-Weg 3, D-37077 Göttingen, Germany
[5] Rosseland Centre for Solar Physics, University of Oslo, P.O. Box 1029 Blindern, NO-0315 Oslo, Norway
[6] ASI, Italian Space Agency, Via del Politecnico snc, I-00133, Rome, Italy
[7] Plasma Dynamics Group, School of Mathematics and Statistics, University of Sheffield, Sheffield, UK
Received 2021 October 15; revised 2021 December 8; accepted 2021 December 19; published 2022 March 10

Abstract

The electromagnetic energy flux in the lower atmosphere of the Sun is a key tool to describe the energy balance of the solar atmosphere. Current investigations on energy flux in the solar atmosphere focus primarily on the vertical electromagnetic flux through the photosphere, ignoring the Poynting flux in other directions and its possible contributions to local heating. Based on a realistic Bifrost simulation of a quiet-Sun (coronal hole) atmosphere, we find that the total electromagnetic energy flux in the photosphere occurs mainly parallel to the photosphere, concentrating in small regions along intergranular lanes. Thereby, it was possible to define a proxy for this energy flux based on only variables that can be promptly retrieved from observations, namely, horizontal velocities of the small-scale magnetic elements and their longitudinal magnetic flux. Our proxy accurately describes the actual Poynting flux distribution in the simulations, with the electromagnetic energy flux reaching 10^{10} erg cm^{-2} s^{-1}. To validate our findings, we extended the analysis to SUNRISE/IMaX data. First, we show that Bifrost realistically describes photospheric quiet-Sun regions, as the simulation presents similar distributions for line-of-sight magnetic flux and horizontal velocity field. Second, we found very similar horizontal Poynting flux proxy distributions for the simulated photosphere and observational data. Our results also indicate that the horizontal Poynting flux in the observations is considerably larger than the vertical electromagnetic flux from previous observational estimates. Therefore, our analysis confirms that the electromagnetic energy flux in the photosphere is mainly horizontal and is most intense in localized regions along intergranular lanes.

Unified Astronomy Thesaurus concepts: Solar chromospheric heating (1987); Magnetohydrodynamics (1964); Solar surface (1527); Solar magnetic fields (1503); Solar granulation (1498)

1. Introduction

Essential aspects of energy generation, transport, and dissipation responsible for the heating of the upper atmosphere of the Sun remain elusive. Although the ongoing turbulent motion in the upper convective zone, particularly in the intergranular lanes (Pontin & Hornig 2020), can be considered a natural reservoir of energy for heating the upper solar atmosphere, the question remains of how this energy can be transferred to the higher regions. By shuffling the magnetic field lines, the convective motions would be able to increase sufficiently the magnetic energy to compensate for coronal and chromospheric energy losses, driving injection of magnetic energy later transformed into heating by AC or DC mechanisms. The magnetic nature of the solar atmosphere's dynamics and the magnetic coupling between different heights indicate the flux of electromagnetic energy, i.e., the Poynting flux, as the primary mechanism for energy transport (Nordlund et al. 2009; Shelyag et al. 2012).

The electromagnetic energy flux input in the upper solar atmosphere is described by the vertical component of the Poynting flux produced by vertical plasma motions transporting horizontal magnetic field and the work done by horizontal motions on the vertical magnetic field (Shelyag et al. 2012). The importance of vertical and horizontal plasma velocities to the upward Poynting flux depends on the magnetic configuration of the solar atmosphere. Based on realistic MHD simulations of the lower atmosphere, Steiner et al. (2008) found that a positive vertical component of the Poynting flux in the photosphere could be provided by horizontal magnetic fields expelled to the upper photosphere by convective overshooting. For a simulated solar plage, Shelyag et al. (2012) found that the horizontal motions of the solar photospheric vortices would be the primary sources of vertical Poynting flux, encompassing regions with intense electromagnetic energy flux going up and down, but resulting in a total positive net. Besides playing an essential role in generating an upward-pointing Poynting flux, the small-scale vortices could provide enough energy to heat the chromosphere (Yadav et al. 2020). The swirling motions in the chromosphere also provide a mean net upwardly directed Poynting flux and can spatially correlate to intense vertical Poynting flux distributions (Battaglia et al. 2021).

In active regions, a strong correlation between the averaged X-ray brightness and a proxy for Poynting flux was first suggested by Fisher et al. (1998). Tan et al. (2007) confirmed that correlation and found the Poynting flux to be in the range of $10^{6.7}$–$10^{7.6}$ ergs cm^{-2} s^{-1}, which provides enough energy to justify coronal temperatures. According to estimates based on observational data, the upward Poynting flux can also provide the necessary energy input in solar plage regions (Yeates et al. 2014; Welsch 2015).

The Poynting flux input from the photosphere is not constant and tends to strongly vary as a function of time (Shelyag et al. 2012; Hansteen et al. 2015). The highly variable nature of the vertical Poynting flux results from the Poynting flux magnitude being regulated by the angle between the magnetic field and the solar surface, which tends to fluctuate as the magnetic field lines are dragged and twisted by photospheric motions. The dependency on magnetic energy and the plasma velocity transporting the energy is also one of the causes for the high variability of the Poynting flux. Thereby, a complete description of the Poynting vector in the photosphere is an essential aspect for an accurate description of the electromagnetic energy transport in the solar atmosphere. However, those dependencies of the Poynting flux make observational estimates highly dependent on both the methodology to recover photospheric velocity and the assumptions used to describe the 3D electromagnetic field in the photosphere (Fisher et al. 2012; Kazachenko et al. 2014; Welsch 2015). Another challenge is that the analysis on solar energy transport only considered a narrow class of plasma motions, neglecting the complexity of plasma flows and their capacity to reorganize the magnetic field. Sakaue & Shibata (2020) found that intermediate shock regions can reduce transmission of the Poynting flux by Alfvén waves; therefore, it is not well established how much of the energy generated by photospheric motions will reach the chromosphere and solar corona.

Based on realistic Bifrost simulation of a quiet-Sun atmosphere, our work focuses on an approximate description of the total Poynting flux for the wealthy dynamics of photospheric plasma flow. We show that the total Poynting flux can be evaluated from an approximation that relies only on physical plasma variables that can be established from observations: horizontal plasma motions, as derived from tracking magnetic elements, and line-of-sight magnetic flux obtained from spectropolarimetric inversions. We extend our analysis to observations using SUNRISE/IMaX data and validate the simulation findings. Although our approximation for Poynting flux estimations has been previously applied to describe upward electromagnetic energy flux in active regions (Fisher et al. 1998; Tan et al. 2007), we demonstrate that such a proxy, in reality, describes the horizontal Poynting flux with considerable accuracy. Moreover, our analysis clearly shows that the vertical electromagnetic energy flux is only a small fraction of the total Poynting flux. Our findings also indicate the upper photosphere and lower chromosphere as the regions with higher contributions for upward electromagnetic energy flux, suggesting those regions as the most likely energy sources in the upper atmosphere. Our paper is organized as follows: Section 2 describes the Bifrost simulation and the methodology to retrieve the velocity field from SUNRISE/IMaX observations; Section 3 presents the description of the photospheric Poynting flux, our approximation for observation of the Poynting flux, and the validation of our findings based on SUNRISE/IMaX data. Finally, Section 4 presents a discussion of our results and conclusions on our findings.

2. Methodology

2.1. Bifrost Simulations

The numerical data used in our study were obtained using the Bifrost code (Gudiksen et al. 2011), which simulates realistic magnetoconvection in the solar photosphere and upper convection zone based on radiative MHD equations. The simulation domain consists of $768 \times 768 \times 768$ grid cells, covering 24 Mm in the x- and y-directions and 16.8 Mm in the vertical z-direction, with 31 km horizontal resolution and 12–82 km variable vertical resolution. The simulated atmosphere reaches up the lower corona, extending vertically to 14.3 Mm above the surface. The model used in the numerical approximation realistically mimics a coronal hole (i.e., a quiet-Sun region with open fields in the upper atmosphere), consisting of only small-scale opposite-polarity magnetic fields in the photosphere with an average signed field strength of 5 G and a mean unsigned field strength of 40 G. Thereby, the Bifrost data set adequately represents regions with predominantly vertical magnetic fields. The visible solar surface (Rosseland optical depth $\tau = 1$) is located at 2.5 Mm above the lower boundary. At the bottom boundary, a horizontal field of 200 G along the y-axis was fed into the inflows in a way that the magnetic field strength is slowly increasing with time and there are interactions between the existing field and the flux emergence. The top and bottom boundaries of the simulation box are transparent, and the lateral boundaries are periodic. The radiative transfer equations in the photosphere and low chromosphere take into account scattering (Skartlien 2000), and the chromospheric (and transition region) radiative losses are computed in non-LTE conditions (Carlsson & Leenaarts 2012); Hydrogen ionization in this simulation is treated in LTE. For further details we refer to De Pontieu et al. (2021), where the same simulation run (with identity number ch024031_by200bz005) has also been analyzed.

Figure 1 shows the simulated atmosphere at time 76′ 46″. In the left panel, we see the whole domain, and the lower horizontal plane is placed 26 km above the simulated solar surface colored by the continuum intensity. The horizontal domain covers multiple granules and their intergranular regions, an important part of our Poynting flux analysis. In the upper horizontal plane, placed at 1.9 Mm above the surface, we see the distribution of the vertical velocity field, v_z. Although it is not the scope of our analysis, it is interesting to point out that these Bifrost data also simulate the chromospheric swirls, as indicated by the ring shapes formed in v_z. The white cuboid shows the region used for close view of the simulated domain, and the magnetic field topology for that region is shown in the right panel of Figure 1. The horizontal plane is placed 26 km above the simulated surface and is color-coded by the z-component of the magnetic field. The magnetic field lines are traced from random uniformly distributed points in the simulated photosphere, and they are colored by their inclination with respect to the vertical direction. The magnetic field lines display a wealthy topology, being mainly horizontal in the regions lying close to the surface and presenting twists and lower inclination at upper heights.

2.2. SUNRISE/IMaX Observations

To validate our analysis based on the simulation data set and estimate the Poynting flux in the photosphere, we extend our investigation to observational data. More specifically, a seeing-free spectropolarimetric data set obtained by the Imaging Magnetograph eXperiment (IMaX; Martínez Pillet et al. 2011) on board the first flight of the SUNRISE balloon-borne solar observatory (Solanki et al. 2010; Barthol et al. 2011; Berkefeld et al. 2011) is being analyzed. The data were acquired on 2009 June 9 and consist of 32 minutes (for a total of 100 scans) of full Stokes measurements along the Fe I 525.02 nm spectral line

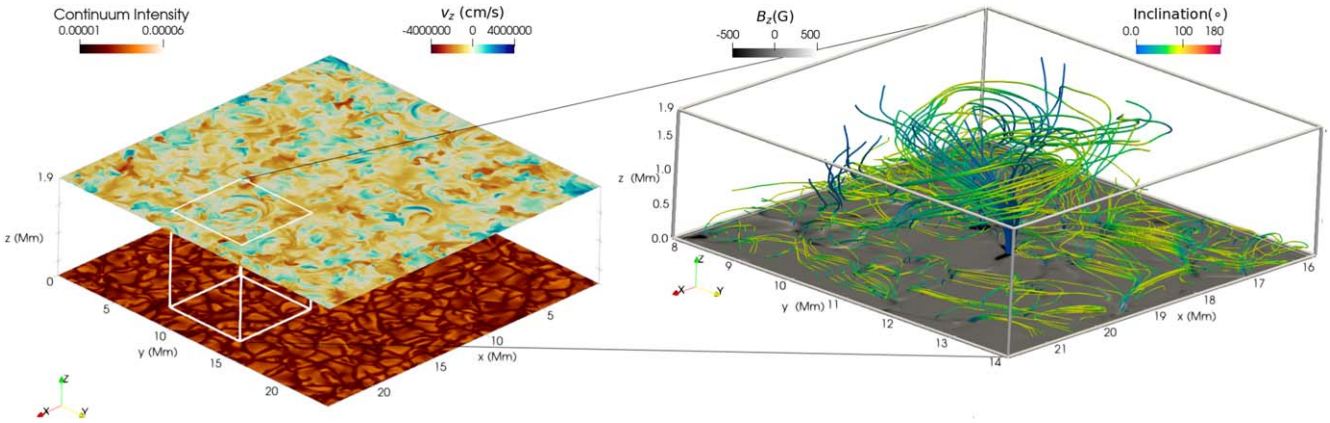

Figure 1. The Bifrost simulation domain. Left panel: the (x, y) planes are placed 26 km above the simulated solar surface, colored by the continuum intensity, and 1.9 Mm above the surface, colored by the vertical component of the velocity field. The white cuboid shows the region used for close view of the simulated domain. Right panel: depiction of the magnetic field lines for the region in the white cuboid from the left panel. The (x, y) plane is placed 26 km above the simulated solar surface, colored by the z-component of the magnetic field saturated at 500 G. The magnetic field lines are colored by the inclination of the magnetic field.

(in four wavelength positions in the line and one in the continuum) with a cadence of 33 s and a spatial sampling of $0\farcs0545$ pixel^{-1}. The data were phase-diversity reconstructed, reaching to a (single-position) noise level of $\approx 3 \times 10^{-3}$ in the units of Stokes I continuum. The field of view (FOV) is approximately 40×40 arcsec^2 and samples a quiet-Sun region at disk center. In our study we used the results of the Stokes inversion previously presented by Kianfar et al. (2018). In particular, the longitudinal component of the magnetic field strength, retrieved by the SPINOR inversion code (Frutiger et al. 2000; Berdyugina et al. 2003), was used to estimate the Poynting flux vector. For further details on the Stokes inversion procedure we refer the reader to Kianfar et al. (2018) and Kahil et al. (2017).

For our analysis, the photospheric horizontal velocity, v_h, was retrieved from the SUNRISE/IMaX observations based on tracking the magnetic elements detected in the data using the SWAMIS[8] (DeForest et al. 2007) code. The same analysis was also applied to the simulation data (at 115 km above the solar surface) in order to compare the results. The SWAMIS algorithm works by

1. Detecting: magnetic elements are identified in each image.
2. Identifying: the detected elements are given a unique identification number.
3. Associating: the elements in one image are associated with the same elements in the preceding and following images.

In the case of SUNRISE/IMaX data, the code tracks and identifies groups of pixels in the circular polarization (CP) maps. For the simulation data, we convolved the vertical magnetic field (B_z) with a point-spread function (PSF) similar to the IMaX one, and we use this resulting map as input for the magnetic tracking. The SUNRISE/IMaX CP maps are constructed from the Stokes V signals pixel-wise, following the method set out by Martínez Pillet et al. (2011):

$$\mathrm{CP} = \frac{1}{4\langle I_c \rangle} \sum_{i=1}^{4} \epsilon_i V_i, \tag{1}$$

where $\epsilon_{1,2} = 1$ for the first two spectral positions of the line sampling (i.e., in the blue wing) and $\epsilon_{3,4} = -1$ for the next two positions (i.e., in the red wing). In the above equation I_c is the normalization factor applied to the Stokes V profiles, and it is derived taking the Stokes I continuum intensity (i.e., the fifth wavelength position) over each corresponding pixel. The CP has a considerably lower noise level of 1.7×10^{-3} I_c (Jafarzadeh et al. 2014), and thus a larger signal-to-noise ratio (compared to the signal of the single Stokes V wavelength positions), facilitating the detection of small-scale magnetic structures.

The SWAMIS code uses a two-threshold (high and low) signed discriminator. These thresholds are chosen as 2σ and 6σ, respectively, where σ corresponds to the standard deviation of the magnetic signal over the FOV for the SUNRISE/IMaX's CP and B_z simulation maps. Then, we selected suitable and representative magnetic elements on the basis of their lifetimes (longer than 10 consecutive frames) and sizes (minimum 8 pixels), and we estimated their instantaneous horizontal velocity, v_h, by tracking their positions in time.

The SUNRISE/IMaX data at photospheric heights are shown in Figure 2. In particular, this figure displays (from the bottom to the top) the continuum intensity, the magnetic field as retrieved by the SPINOR inversion, and the CP maps. The magnetic elements that fulfill the SWAMIS code's criteria are shown in orange at the top (x, y) plane. As shown by Figure 2, the code identifies all the pixels with a magnetic signal from the CP, which are direct measurements of the magnetic field along the line of sight.

Finally, we employed the DeepVel method[9] developed by Asensio Ramos et al. (2017) to estimate the instantaneous horizontal velocities, v_h, at all pixels over the entire FOV of the SUNRISE/IMaX data. Deepvel is a deep neural network that optimizes its network weights by considering the outputs and inputs from the two ends through convolution using a series of transformations that relates the transverse velocities' vector field (the output) to the maps of the intensity I_c (input) at the surface. The Deepvel applied in this paper was already trained for the IMaX images with a 30 s cadence.

[8] Available at https://www.boulder.swri.edu/swamis/.

[9] Available at https://github.com/aasensio/deepvel.

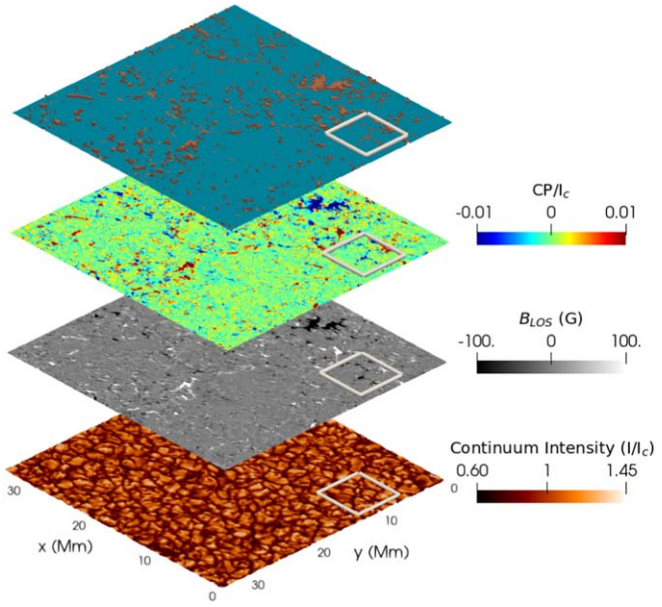

Figure 2. From bottom to top: IMaX continuum intensity, magnetic field obtained from SPINOR inversions saturated at 100 G, IMaX CP maps, and magnetic elements depicted in orange. The white box indicates the sub-FOV shown in Figure 6.

3. Results

3.1. Electromagnetic Energy Flux in the Solar Atmosphere

The electromagnetic energy flux is described by the magnetic Poynting vector, which can be written in MHD approximation as

$$\boldsymbol{S} = \frac{1}{4\pi}\boldsymbol{B} \times (\boldsymbol{v} \times \boldsymbol{B}), \tag{2}$$

where $\boldsymbol{v}$ is the plasma velocity and $\boldsymbol{B}$ is the magnetic field. To describe the energy flux orientation in relation to the magnetic field, we write the velocity field in terms of its parallel ($\boldsymbol{v}_{\parallel}$) and perpendicular ($\boldsymbol{v}_{\perp}$) components to $\boldsymbol{B}$. As a result, Equation (2) becomes

$$\boldsymbol{S} = \frac{1}{4\pi}\boldsymbol{v}_{\perp}(\boldsymbol{B} \cdot \boldsymbol{B}). \tag{3}$$

Therefore, the electromagnetic energy flux can be interpreted as magnetic energy density transported by the portion of the plasma velocity flowing perpendicular to the magnetic field. The above expression includes the contributions from transverse waves, as the transverse perturbations in the magnetic field lead to creation of horizontal components of the magnetic field and thereby a vertical component for the Poynting flux and thus energy transport in the vertical direction. Equation (3) also indicates that the transport of electromagnetic energy to the upper atmosphere requires magnetic field lines with inclination with respect to the vertical direction.

The first hint on electromagnetic energy flux in the lower atmosphere is provided in a close view, 6.25×6.25 Mm, of a horizontal plane at $\sim$115 km above the simulated solar surface as displayed in Figure 3. The granular patterns of the region are indicated by the vertical component of the velocity field, v_z, in Figure 3(a). The vertical photospheric magnetic field is shown in Figure 3(b), with the color map saturated at $\pm$1000 G, indicating the magnetic flux concentration of both polarities along the intergranular lanes. Figure 3(c) displays the magnitude of electromagnetic energy flux generated by the photospheric dynamics. Comparing Figures 3(a) and (c), we see that the regions where the magnitude of the Poynting vector reaches maximum values are correlated to the concentration of vertical magnetic fluxes. The inclination of the magnetic field with respect to the vertical direction is depicted in Figure 3(d). One can see that the magnitude of the Poynting vector is still considerable in some regions with higher inclination values, where one may expect upward energy flow according to Equation (3). Figure 3(e) displays the magnitude of the horizontal component of the velocity field, $|v_h|$. We also find some correspondence between regions with moderate to high Poynting flux and intense horizontal plasma motions, even in regions with weak vertical magnetic field. To evaluate the contribution of the horizontal component, $\boldsymbol{S}_h = S_x\boldsymbol{i} + S_y\boldsymbol{j}$, to the total Poynting flux, we write $\boldsymbol{S}^2 = \boldsymbol{S}_h^2 + \boldsymbol{S}_z^2$ and calculate the ratio S_h^2/S^2, as shown in Figure 3(f). Our results show that, except for a minor fraction of the surface, the Poynting flux is flowing mainly in the horizontal direction. By comparing Figures 3(c) and (f), we can see that the maximum electromagnetic energy flux in the photosphere flows parallel to the surface, not in the upward direction.

The distribution of the orientation of magnetic field at the photospheric level, i.e., up to 390 km from the solar surface, is indicated in the histogram in Figure 4(a), where we computed B_z^2/B^2. This histogram indicates that the simulated photospheric magnetic field has mostly high inclination. The vertical component of the magnetic field, B_z, is the principal component of the magnetic field in photospheric regions presenting concentrated flux of electromagnetic energy, as indicated in Figure 4(b), where we plot the average value of B_z^2/B^2 in regions $\log_{10}(|S|) > 0.9\log_{10}(S_{\max})$ as a function of height, with $S_{\max}$ being the maximum value for Poynting flux at each height level. Thereby, even though only a small portion of the magnetic field is aligned in the vertical direction, the Poynting flux is mainly originated by the vertical magnetic field in the lower photosphere. In contrast, closer to the chromosphere, the contribution of other magnetic components to the electromagnetic energy flux tends to increase. This indicates that most of the upflow of electromagnetic energy from the photosphere is originated slightly farther from the surface.

The dominant role of vertical magnetic field in contributing to the total electromagnetic energy flux indicates that the photospheric Poynting vector can be mostly retrieved from its horizontal component, $\boldsymbol{S}_h$. The horizontal nature of the Poynting vector is confirmed in Figure 4(c), where we plot the frequency distribution of the contribution of the horizontal Poynting vector to the total electromagnetic energy flux, S_h^2/S^2, for up to around 390 km above the solar surface. Figure 4(c) shows that, close to the solar surface, only a tiny fraction of the electromagnetic energy generated by photospheric dynamics is flowing to the upper solar atmosphere or going back under the surface. The electromagnetic energy in the low photosphere will mostly flow within that height range. The S_h^2/S^2 frequency distribution compared to the B_z^2/B^2 histogram, panel (a), indicates that even magnetic fields with some inclination will likely not lead to upflows of electromagnetic energy. In other words, in those cases the electromagnetic energy tends to flow perpendicular to the magnetic field along the plane defined by inclined magnetic fields. In

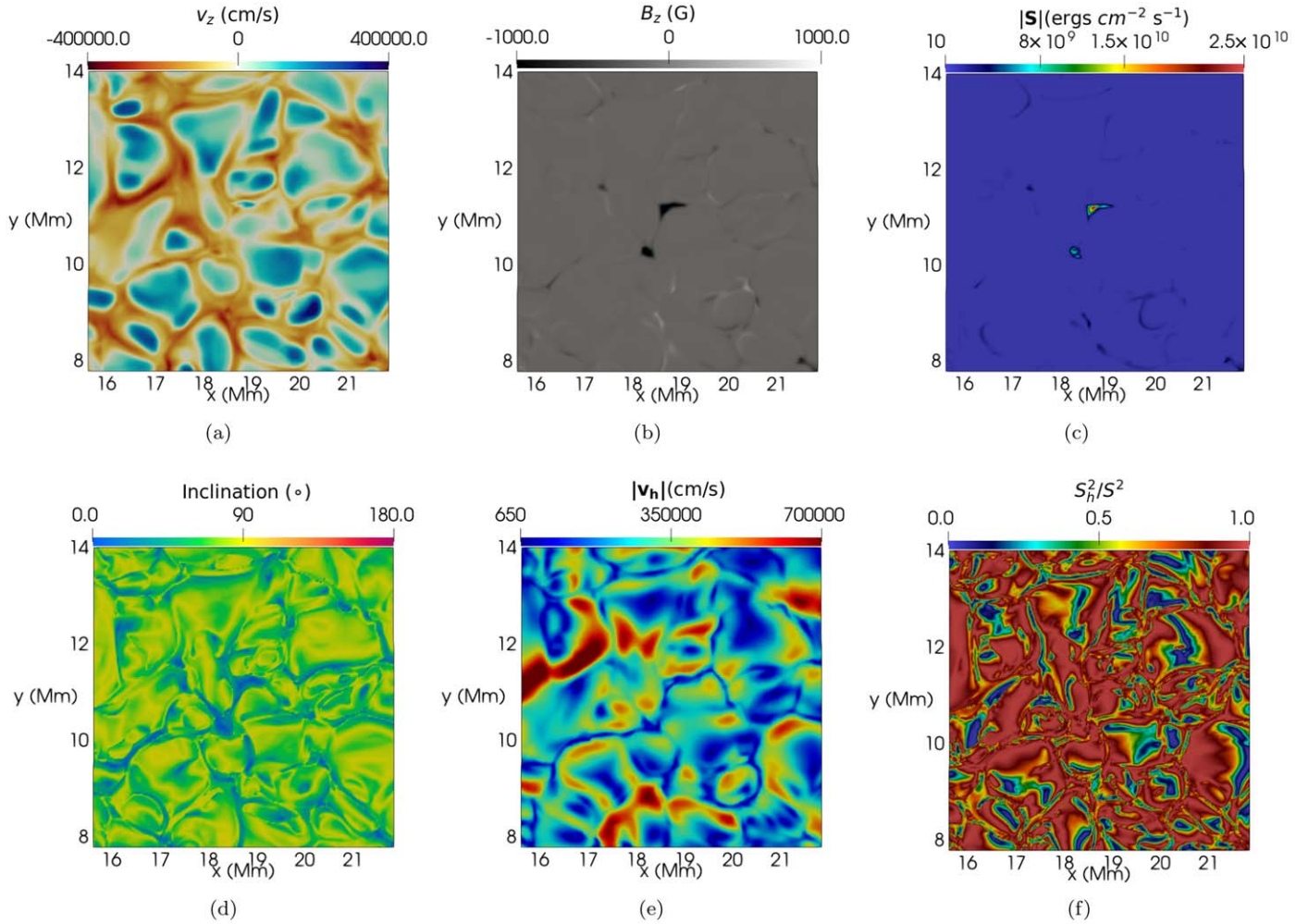

Figure 3. Close view of a 6.25 ×6.25 Mm^2 region from the Bifrost simulation indicated by the white rectangle in Figure 1. The horizontal planes are placed ∼115 km above the solar surface. The individual panels illustrate (a) the vertical component of the velocity field, (b) the vertical component of the magnetic field, (c) the magnitude of the Poynting flux, (d) the inclination of the magnetic field, (e) the horizontal plasma velocity, and (f) the ratio S_h^2/S^2.

parts of the flow where we have considerable electromagnetic energy flux, $\log_{10}(|S|) > 0.9\log_{10}(S_{\max})$, the Poynting flux vector has a dominant horizontal component, as indicated by the average value of S_h^2/S^2 as a function of height displayed in Figure 4(d).

3.2. Defining an Approximation to the Poynting Vector

The above findings indicate that in regions with high concentration of electromagnetic energy fluxes we can approximate the Poynting flux as

$$\boldsymbol{S} \sim \boldsymbol{S}_h \sim \frac{1}{4\pi}\boldsymbol{v}_h(\boldsymbol{B}\cdot\boldsymbol{B}) = \frac{1}{4\pi}\boldsymbol{v}_h(B_x^2 + B_y^2 + B_z^2). \quad (4)$$

The approximation presented in Equation (4) is still challenging to current observational data, as it depends on the horizontal component of the magnetic field. Despite the quiet-Sun area being also characterized by the transverse component of the magnetic field (Jafarzadeh et al. 2014; Bellot Rubio & Orozco Suárez 2019), these measurements are still limited owing to the limited spatial resolution and polarimetric accuracy of the present instrumentation. Figure 4(a) shows that the contribution from the horizontal component of the magnetic field can be disregarded for some regions, especially for regions where $\log_{10}(|S|) > 0.9\log_{10}(S_{\max})$ as depicted in Figure 4(b). Therefore, we can further approximate Equation (4) by

$$\boldsymbol{S}^{\rm obs} \sim \frac{1}{4\pi}\boldsymbol{v}_h B_z^2, \quad (5)$$

where $\boldsymbol{S}^{\rm obs}$ is the observable Poynting flux, i.e., an estimation for Poynting flux based solely on quantities that can be easily retrieved from solar observational data. The above expression is rather similar to the approximation made before by Fisher et al. (1998) and Tan et al. (2007) when estimating the Poynting flux in active regions. However, those studies actually applied the approximation in Equation (5) to estimate the electromagnetic energy flowing upward.

To evaluate the validity of Equation (5), we applied our approximation in conjunction with our simulation data and compared the magnitude of $\boldsymbol{S}^{\rm obs}$ to the total magnitude of the Poynting flux obtained using Equation (2). Figure 5(a) displays the distribution of the Poynting flux derived from the simulation, as described by Equation (3) (brown histogram) and with the approximation using Equation (5) (blue distribution). We find that the approximation described by Equation (5) is able to accurately capture the distribution of Poynting flux in the photosphere. For the regions where $\log_{10}(|S|) > 0.9\log_{10}(S_{\max})$, the relative error

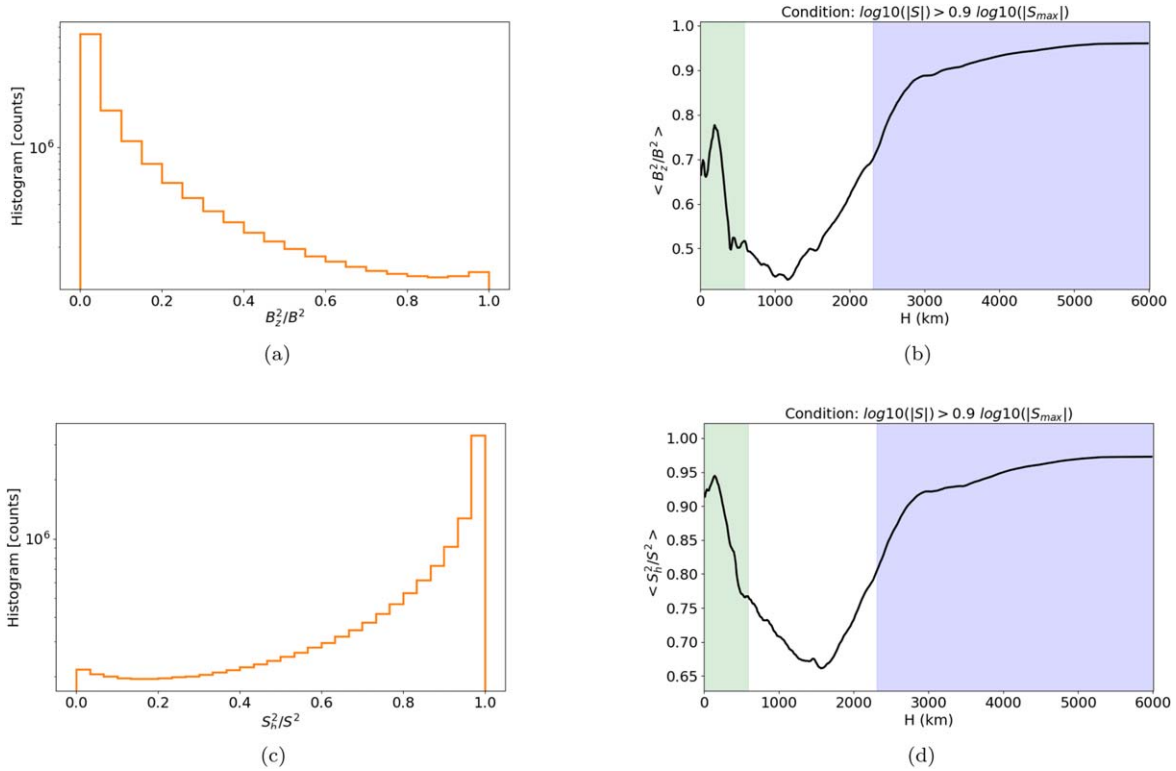

Figure 4. Left panels: distribution of B_z^2/B^2 (panel (a)), and the distribution of the ratio S_h^2/S^2 (panel (c)) from the solar surface up to a height of ~390 km. Right panels: average value of B_z^2/B^2 (panel (b)) and S_h^2/S^2 (panel (d)) for regions where $\log_{10}(|S|) > 0.9\log_{10}(S_{\max})$ as a function of height. The colors indicate the average height range of the photosphere (green), chromosphere (white), and transition region and corona (purple).

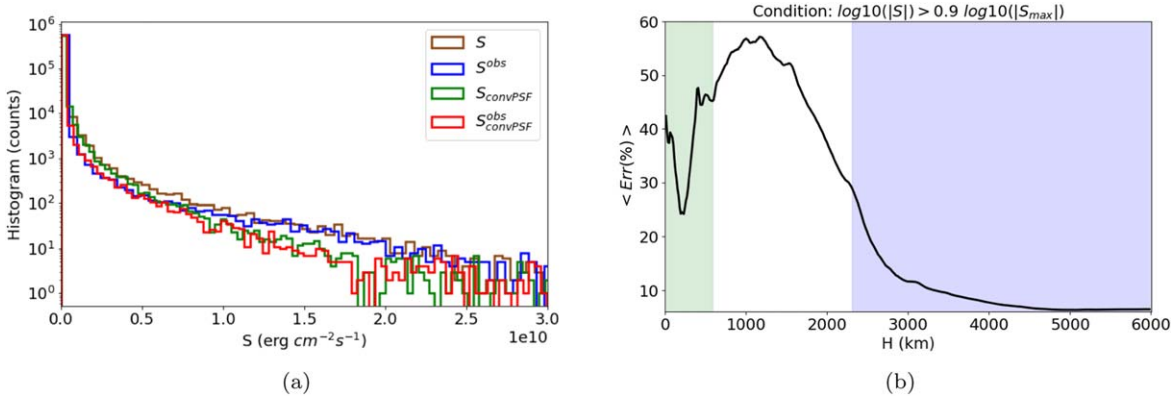

Figure 5. (a) Distribution of the Poynting flux derived from the simulation as described by Equation (3) (blue histogram) and with the approximation (brown distribution) using Equation (5). The red/green distributions have been obtained by convolving the original simulation with the IMaX PSF. (b) Average value of the relative error, *Err*, for regions where $\log_{10}(|S|) > 0.9\log_{10}(S_{\max})$ as a function of height.

between $S_{\rm obs}$ and S is, on average, lower than 23.4% in the photosphere as displayed in Figure 5(b). Finally, for a better comparison between the simulation and the observations, we convolved the simulation with a PSF with a width comparable that of the IMaX instrument. These results are displayed in Figure 5(a) as green and red histograms, respectively. Our results show a great agreement for the approximated and total Poynting flux.

3.3. Comparison with Observational Data

Figure 6 displays a magnification of the SUNRISE/IMaX area inside the white cuboid shown in Figure 2. We have applied the Deepvel method to retrieve the horizontal plasma motion from observations and thereby compute the Poynting flux at each spatial position according to Equation (5). We display maps of the vertical components of the velocity and magnetic field (panels (a) and (b)), Poynting flux vector (panel (c)), magnetic field inclination (panel (d)), and horizontal component of the velocity field (panel (e)). These maps show that both the simulation and observation have a similar spatial distribution for the displayed variables, except for the inclination map. This discrepancy is caused by the limitations of inversion procedures. This map is noisier than the simulation one with less spatial structuring owing to the noisy Q and U Stokes profiles in the quiet-Sun area. It is worth noting that the map in Figure 6(c) shows that the observational photospheric Poynting flux spatial distribution is very similar to what was found in the simulation data. The Poynting flux tends to be intense and

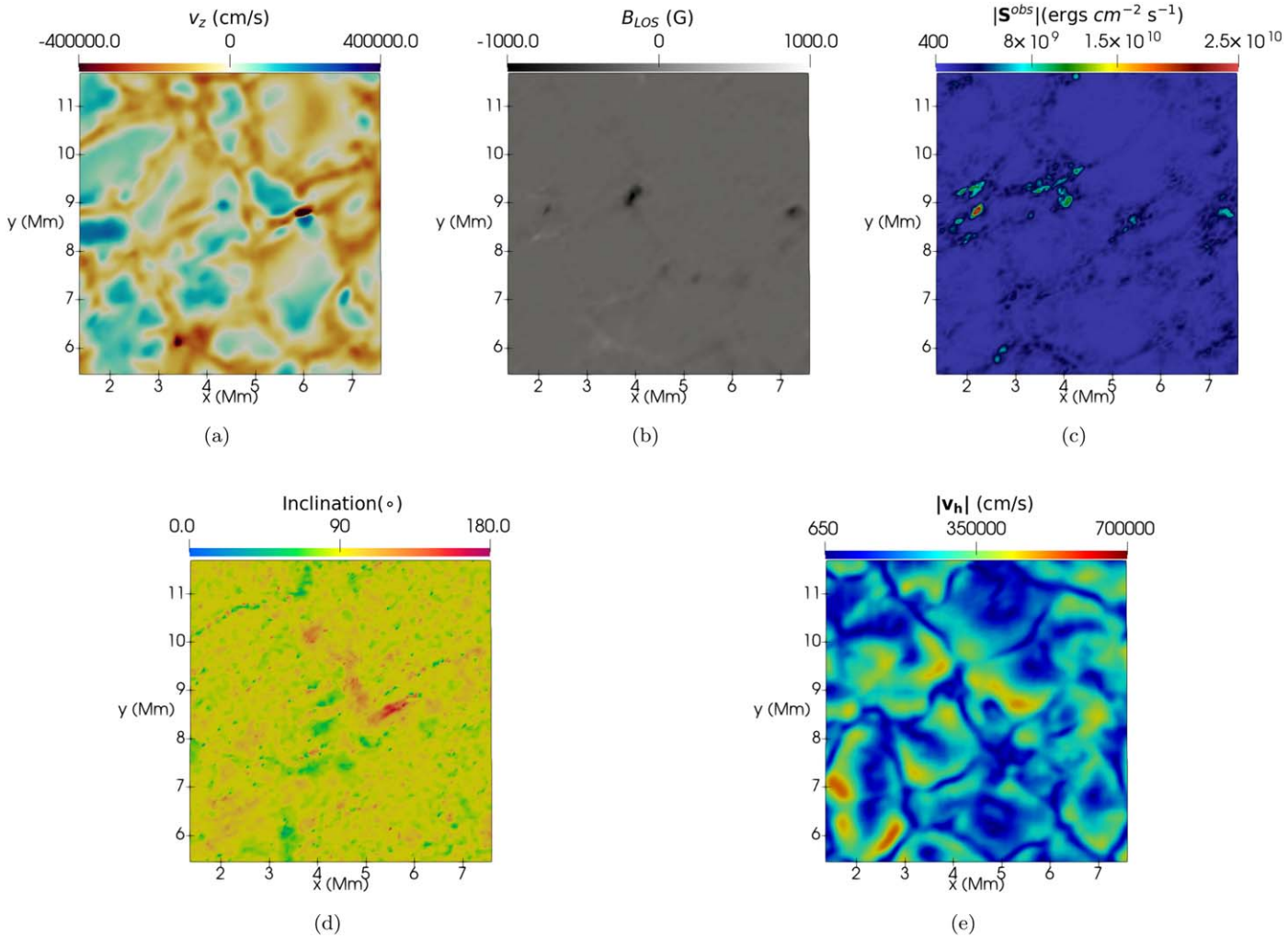

Figure 6. Close view of a ∼6.2 × 6.2 Mm region from the IMaX observation indicated by the white rectangle in Figure 2: (a) the vertical component of the velocity field; (b) the vertical component of the magnetic field; (c) the magnitude of the proxy of the Poynting flux; (d) the magnetic field inclination; (e) the horizontal plasma velocity.

localized in small regions along the intergranular lanes, cospatial with line-of-sight magnetic field concentrations. The Deepvel horizontal velocity map displays a pattern resembling the granulation with values lower than those of the simulation data, even though the values are still greater than 3 km s^{-1}.

Through the feature tracking we obtained the horizontal velocity and the horizontal Poynting flux associated with each magnetic elements in both the IMaX and Bifrost data. In particular, Figure 7 (a) displays the resulting horizontal velocity, v_h, showing that comparable results were found for the v_h retrieved using both simulation and SUNRISE/IMaX data. We also report for completeness the horizontal velocity of the simulation associated with each magnetic element at 115 km (see green histogram in Figure 7 (a)). For these elements we found a similar horizontal velocity on average between 0.5 and 1 km s^{-1}, in agreement with those reported in earlier studies (Stangalini et al. 2013).

As the Poynting vector also depends on the magnetic field vector, in Figure 7(b) we display the distribution of the magnetic field. Olive and black histograms represent the z-component of the magnetic field associated with each magnetic element for the simulation and the SUNRISE/IMaX data, respectively. The green and blue histograms indicate the B_z component and the total magnetic field of the simulation at 115 km within the entire available FOV, respectively. As can be noted, when we applied the tracking features method, we do not consider two regions: those of the elements with small (less than 150 G) and high (greater than 800 G) values of the magnetic field. The lower limit is due to the smallest scale that our instrumentation can detect. On the other hand, the upper limit is the consequence of the diverse thresholds (spatial and temporal) that we set out. Another important aspect to be noted concerns the small difference between the simulation vertical and total component of the magnetic field. Indeed, the intense magnetic field at photospheric heights is mostly vertical (see the green and blue curves). This further supports the application of our approximation discussed in Section 3.2.

The plots displayed in Figure 7(c) show the distributions of the Poynting vector when we consider the tracked magnetic elements. The distributions present a good agreement, which is expected since we found a comparable horizontal velocity and vertical magnetic field distributions for observations and simulations. Again, for completeness, in panel (c) we plot the Poynting vector derived using the horizontal velocity at 115 km of the simulation associated with each magnetic feature found (green histogram). In Figure 7(d) we compare the

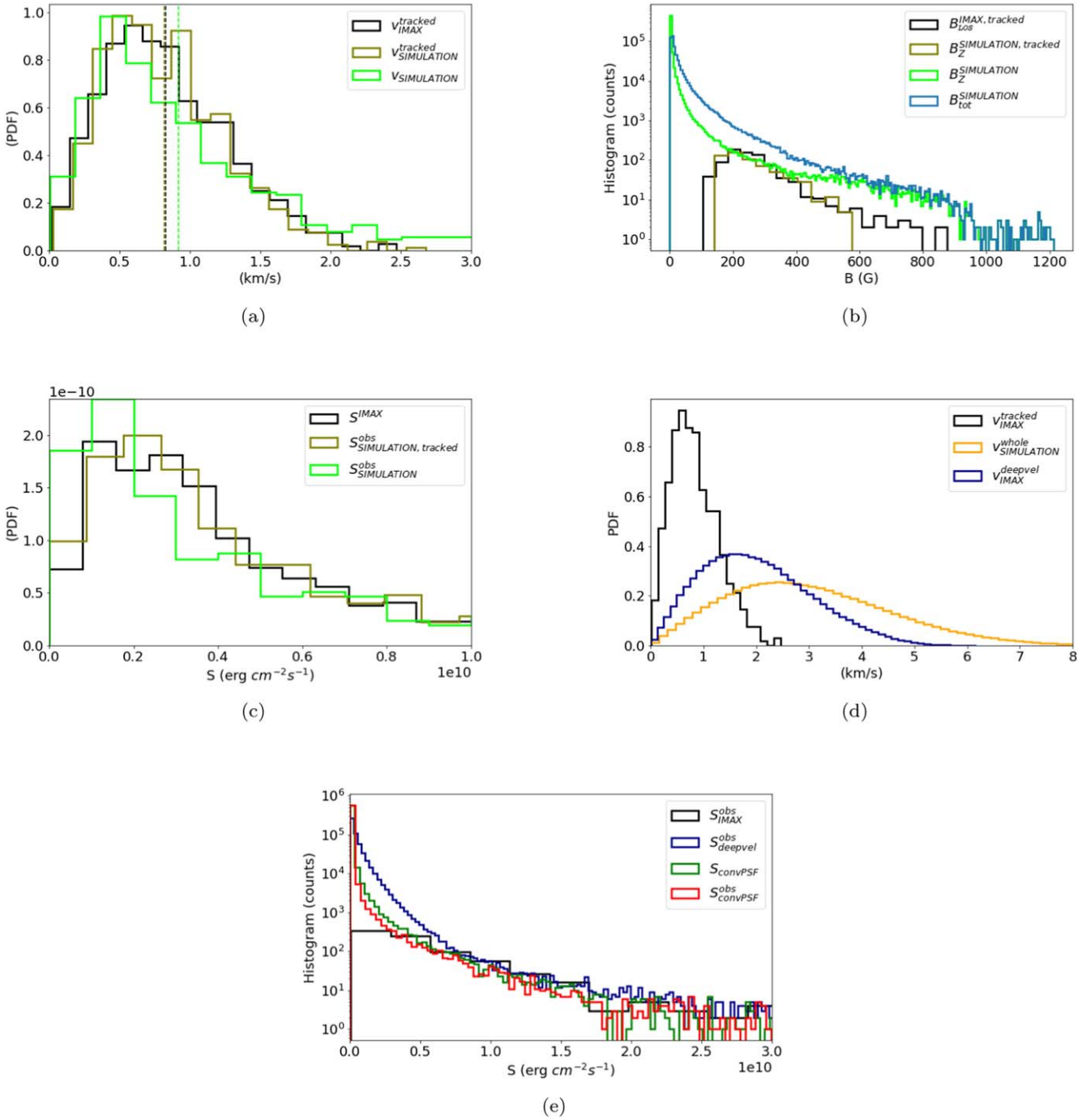

Figure 7. (a) Probability density function of the horizontal velocity field, v_h, associated with the magnetic elements tracked in the IMaX data (black histogram) and the simulation domain (olive histogram). The green distribution represents v_h derived from the simulation at 115 km at the same magnetic elements selected. The three dashed lines indicate the average values of v_h. (b) Distribution of the vertical magnetic field at the magnetic elements in the IMaX (black histogram) and the simulation (olive histogram) data sets. For comparison, considering all pixels of the simulation domain at 115 km (i.e., photospheric heights), we also show B_z and the total magnetic field (green and light-blue histograms). (c) Probability density function of the horizontal Poynting flux calculated by means of Equation (5). (d) Overview of the horizontal velocity of the IMaX data (derived with the two methods; black and blue histograms) and for the simulation (orange histogram). (e) Distribution of the total Poynting flux using Equation (2) ($S_{convPSF}$; green histogram) and the Poynting flux derived using Equation (5) ($S^{obs}_{convPSF}$; red curve). Both quantities are convolved with the IMaX PSF. The black histogram represents the Poynting flux as derived from the IMaX observations, and the blue curve shows the Poynting flux using the value of v_h retrieved with the Deepvel method for the IMaX data.

horizontal velocity retrieved with the two methods (magnetic tracking and Deepvel) of the SUNRISE/IMaX data and the results of simulation. The horizontal velocity associated with the magnetic elements peaks at around 0.8 km s^{-1}, while this result is shifted to higher values when we consider the whole FOV.

Figure 7(e) displays the Poynting vector at each pixel of the whole simulation domain convolved with an opportune PSF with width similar to the IMaX instrument (red histogram) compared to that at the SUNRISE/IMaX magnetic features tracked (black histogram). This plot reveals a good agreement between the two data considered. Furthermore, for comparison, we also overplot

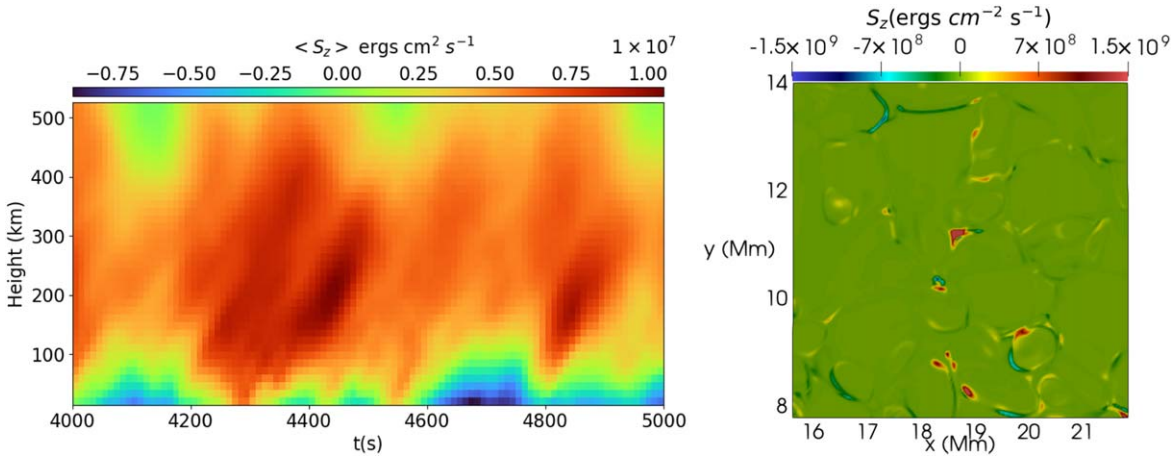

Figure 8. Left panel: the average value of S_z for each height level above the surface, up to 500 km, and for each time frame within a time interval of 1000 s (16.66 minutes). The vertical and horizontal axes indicate the height and time, respectively. Right panel: close view of a 6.25 × 6.25 Mm^2 region from Bifrost simulation indicated by the white rectangle in Figure 1. The horizontal plane is placed around 100 km above the surface, and it is colored by the z-component of the Poynting flux, S_z.

the Poynting vector derived using Equation (3) and the Poynting vector calculated using the Deepvel horizontal velocity at each available spatial position (green and blue histograms, respectively). Except for the low-energy part, all the computations for Poynting vector present a similar behavior. The Poynting vector of the SUNRISE/IMaX data (black histogram) appears flattened at small energy, probably due to the lower limit of detected signal below our capabilities. In this low-energy range the Poynting vector calculated using the Deepvel horizontal velocity has greater values owing to the overestimated horizontal velocity field, intrinsic of this method (Asensio Ramos et al. 2017). Indeed, the neural network was trained with IMaX data with 30 s cadence, instead of the 33 s of the original IMaX cadence. Asensio Ramos et al. (2017) report DeepVel velocities 1.15 times larger in magnitude than the Local Correlation Tracking methodology.

4. Discussions and Conclusions

The electromagnetic energy flow in the lower atmosphere is an essential aspect to describe the dynamics and energy balance of the solar atmosphere. Estimating the energy flux density accurately from observations and determining the direction of that energy flux is crucial for describing accurately the process of plasma heating. Based on realistic simulations from Bifrost, we find that the electromagnetic energy flux occurs practically along the horizontal plane for most of the photospheric region. The dominance of the horizontal component of the energy flux is observed in both the photosphere and other atmospheric layers, being especially higher in regions where we find strong electromagnetic energy concentration and where the magnetic field is mostly vertical. However, our findings do not preclude the existence of a vertical component capable of transporting enough energy to justify chromospheric heating. The left panel of Figure 8 displays the average of the vertical component of the Poynting flux, $\langle S_z \rangle$, for each height level above the surface and for each time frame within a time interval of 1000 s. For heights of 100 km above the solar surface, the net vertical Poynting flux provides a positive energy input for the upper solar atmosphere. As the radiative losses in a chromospheric quiet-Sun region are estimated to be around 4×10^6 ergs cm^{-2} s^{-1} (e.g Withbroe & Noyes 1977; Vernazza et al. 1981), we find that the net S_z is enough to compensate chromospheric losses for 100 km $\leqslant H \leqslant$ 400 km. The right panel of Figure 8 depicts the distribution of the vertical Poynting flux for the Bifrost simulation at the same height and time as Figure 3, $H \sim$ 115 km and $t = 76' 46''$. Comparing Figure 3(c) and the right panel of Figure 8, it is clear that the higher values of vertical Poynting flux are found in the same regions with a local maximum of the total electromagnetic energy flux. Therefore, the estimate of our proxy for Poynting flux can also provide a good estimate of the regions with higher contributions for energy transport in the vertical direction.

As most of the electromagnetic energy is flowing horizontally, energy can be concentrated by vortices as indicated by Shelyag et al. (2012). As the swirling motion perturbs the magnetic lines, it can create a net upward Poynting flux (Shelyag et al. 2012; Yadav et al. 2020). Our results indicate that a magnetic field with a high inclination does not necessarily lead to a dominant vertical component of the Poynting flux. The vertical component of the Poynting vector tends to contribute more to the total energy flux in the upper part of the photosphere and the chromosphere. However, the upper photospheric regions do not necessarily present higher vertical Poynting flux when compared to regions around 100 km above the solar surface. Therefore, the dominance of the horizontal electromagnetic energy flux does not imply a lower vertical energy flow. In a recent study Battaglia et al. (2021) indicated that the upper photosphere and chromospheric swirls can provide a positive energy input.

Based on the horizontal nature of the Poynting vector, we established an approximation for the Poynting flux that requires only the horizontal plasma motion and the vertical component of the magnetic field, quantities retrieved from observations. In other words, our approximation describes the Poynting vector as the magnetic energy from vertical magnetic flux flowing in the direction of the horizontal plasma flow. Our proxy for the Poynting vector can predict the actual Poynting vector magnitude with an underestimation factor less than 23.4% on average for regions with intense electromagnetic energy flux in the photosphere (100 km $\leqslant H \leqslant$ 300 km). In other words, the proxy provides a lower limit for the observed Poynting flux. The height extension where our proxy works with a lower underestimation factor is within what is possible to retrieve from current available data observations. A greater height range analysis would require multiline polarimetric data, which are not available for the quiet

Sun at the moment. This aspect could be theoretically analyzed and might constitute the subject for future investigations.

We found a similar Poynting flux proxy distribution for both simulated and observational data, with maximum values around 10^{10} ergs cm^{-2} s^{-1}. The SUNRISE/IMaX data reach considerably larger values for the Poynting flux when compared to previous estimates found for vertical electromagnetic energy flux based on high-resolution observations of plage magnetic fields (Yeates et al. 2014; Welsch 2015). This is a strong indication that the photospheric electromagnetic energy flux tends to be mainly horizontal in quiet-Sun regions, as our proxy is based on the horizontal component of the Poynting flux. Although our results for the upper atmosphere strongly depend on the magnetic field and plasma flow conditions, our results describe the Poynting vector for magnetic network patches and solar plage regions, where the magnetic field is primarily vertical. The fact that the Poynting flux has a considerably small vertical component in the photospheric region indicates that, even for other magnetic field configurations, it is likely that we are greatly underestimating the total electromagnetic energy flow by only considering the vertical component. Failing to correctly estimate the full Poynting flux in other atmospheric regions may lead to the wrong description of energy transport. Our results suggest that future investigations should concern the full Poynting vector to evaluate its contribution to local heating properly.

V.F., G.V., I.B., and S.S.A.S. are grateful to The Royal Society, International Exchanges Scheme, collaboration with Brazil (IES \ R1 \ 191114) and Spain (IES \ R2 \ 212183). V.F., G.V., and S.S.A.S. are grateful to Science and Technology Facilities Council (STFC) grant ST/V000977/1 and to The Royal Society, International Exchanges Scheme, collaboration with Chile (IE170301). V.F. would like to thank the International Space Science Institute (ISSI) in Bern, Switzerland, for the hospitality provided to the members of the team on "The Nature and Physics of Vortex Flows in Solar Plasmas." This research has also received financial support from the European Union's Horizon 2020 research and innovation program under grant agreement No. 824135 (SOLARNET). S.J. acknowledges support from the European Research Council under the European Union Horizon 2020 research and innovation program (grant agreement No. 682462) and from the Research Council of Norway through its Centres of Excellence scheme (project No. 262622). The German contribution to SUNRISE is funded by the Bundesministerium für Wirtschaft und Technologie through the Deutsches Zentrum für Luft- und Raumfahrt e.V. (DLR), grant No. 50 OU 0401, and by the Innovations fond of the President of the Max Planck Society (MPG). The Spanish contribution has been funded by the Spanish MICINN under projects ESP2006-13030-C06 and AYA2009-14105-C06 (including European FEDER funds). The HAO contribution was partly funded through NASA grant NNX08AH38G. The Bifrost simulations have been run on clusters from the Notur project, and the Pleiades cluster through the computing projects s1061, s2053, and s8305 from the High End Computing (HEC) division of NASA. This study was financed in part by the Coordenação de Aperfeiçoamento de Pessoal de Nível Superior —Brasil (CAPES), Finance Code 88882.316962/2019-01. M. M. acknowledges support from the European Union's Horizon 2020 Research and Innovation 531 program under grant agreement Nos. 824135 (SOLARNET) and 729500 (PRE-EST) and from the Italian MIUR-PRIN grant 2017 "Circumterrestrial Environment: Impact of Sun-Earth Interaction" and by the Istituto NAzionale di Astrofisica (INAF).

ORCID iDs

Suzana S. A. Silva https://orcid.org/0000-0001-5414-0197
Mariarita Murabito https://orcid.org/0000-0002-0144-2252
Shahin Jafarzadeh https://orcid.org/0000-0002-7711-5397
Gary Verth https://orcid.org/0000-0002-9546-2368
Istvan Ballai https://orcid.org/0000-0002-3066-7653
Viktor Fedun https://orcid.org/0000-0002-0893-7346

References

Andrea Francesco, B., Cuissa, C., José Roberto, C., Bossar, F., Antoine, A., & Oskar, S. 2021, A&A, 649, A121
Asensio Ramos, A., Requerey, I. S., & Vitas, N. 2017, A&A, 604, A11
Barthol, P., Gandorfer, A., Solanki, S. K., et al. 2011, SoPh, 268, 1
Bellot Rubio, L., & Orozco Suárez, D. 2019, LRSP, 16, 1
Berdyugina, S. V., Solanki, S. K., & Frutiger, C. 2003, A&A, 412, 513
Berkefeld, T., Schmidt, W., Soltau, D., et al. 2011, SoPh, 268, 103
Carlsson, M., & Leenaarts, J. 2012, A&A, 539, A39
De Pontieu, B., Polito, V., Hansteen, V., et al. 2021, SoPh, 296, 84
DeForest, C. E., Hagenaar, H. J., Lamb, D. A., Parnell, C. E., & Welsch, B. T. 2007, ApJ, 666, 576
Fisher, G. H., Longcope, D. W., Metcalf, T. R., & Pevtsov, A. A. 1998, ApJ, 508, 885
Fisher, G. H., Welsch, B. T., & Abbett, W. P. 2012, SoPh, 277, 153
Frutiger, C., Solanki, S. K., Fligge, M., & Bruls, J. H. M. J. 2000, A&A, 358, 1109
Gudiksen, B. V., Carlsson, M., Hansteen, V. H., et al. 2011, A&A, 531, A154
Hansteen, V., Guerreiro, N., Pontieu, B. D., & Carlsson, M. 2015, ApJ, 811, 106
Jafarzadeh, S., Solanki, S. K., Lagg, A., et al. 2014, A&A, 569, A105
Kahil, F., Riethmüller, T. L., & Solanki, S. K. 2017, ApJS, 229, 12
Kazachenko, M. D., Fisher, G. H., & Welsch, B. T. 2014, ApJ, 795, 17
Kianfar, S., Jafarzadeh, S., Mirtorabi, M. T., & Riethmüller, T. L. 2018, SoPh, 293, 123
Martínez Pillet, V., Del Toro Iniesta, J. C., Álvarez-Herrero, A., et al. 2011, SoPh, 268, 57
Nordlund, Å., Stein, R. F., Asplund, M., et al. 2009, LRSP, 6, 2
Pontin, D. I., & Hornig, G. 2020, LRSP, 17, 5
Sakaue, T., & Shibata, K. 2020, ApJ, 900, 120
Shelyag, S., Mathioudakis, M., & Keenan, F. P. 2012, ApJL, 753, L22
Skartlien, R. 2000, ApJ, 536, 465
Solanki, S. K., Barthol, P., Danilovic, S., et al. 2010, ApJL, 723, L127
Stangalini, M., Solanki, S. K., Cameron, R., & Martínez Pillet, V. 2013, A&A, 554, A115
Steiner, O., Rezaei, R., Schaffenberger, W., & Wedemeyer-Böhm, S. 2008, ApJL, 680, L85
Tan, C., Jing, J., Abramenko, V. I., et al. 2007, ApJ, 665, 1460
Vernazza, J. E., Avrett, E. H., & Loeser, R. 1981, ApJS, 45, 635
Welsch, B. T. 2015, PASJ, 67, 18
Withbroe, G. L., & Noyes, R. W. 1977, ARA&A, 15, 363
Yadav, N., Cameron, R. H., & Solanki, S. K. 2020, ApJL, 894, L17
Yeates, A. R., Bianchi, F., Welsch, B. T., & Bushby, P. J. 2014, A&A, 564, A131